Ephemerality of discrete methane vents in lake sediments

Benjamin P. Scandella[1], Liam Pillsbury[2], Thomas Weber[2], Carolyn Ruppel[3,4], Harold F. Hemond[1], and Ruben Juanes[1,4]

[1]Department of Civil and Environmental Engineering, Massachusetts Institute of Technology, Cambridge, Massachusetts, USA, [2]Department of Mechanical Engineering, University of New Hampshire, Durham, New Hampshire, USA, [3]U.S. Geological Survey, Woods Hole, Massachusetts, USA, [4]Department of Earth, Atmospheric and Planetary Sciences, Massachusetts Institute of Technology, Cambridge, Massachusetts, USA

Abstract Methane is a potent greenhouse gas whose emission from sediments in inland waters and shallow oceans may both contribute to global warming and be exacerbated by it. The fraction of methane emitted by sediments that bypasses dissolution in the water column and reaches the atmosphere as bubbles depends on the mode and spatiotemporal characteristics of venting from the sediments. Earlier studies have concluded that hot spots—persistent, high-flux vents—dominate the regional ebullitive flux from submerged sediments. Here the spatial structure, persistence, and variability in the intensity of methane venting are analyzed using a high-resolution multibeam sonar record acquired at the bottom of a lake during multiple deployments over a 9 month period. We confirm that ebullition is strongly episodic, with distinct regimes of high flux and low flux largely controlled by changes in hydrostatic pressure. Our analysis shows that the spatial pattern of ebullition becomes homogeneous at the sonar's resolution over time scales of hours (for high-flux periods) or days (for low-flux periods), demonstrating that vents are ephemeral rather than persistent, and suggesting that long-term, lake-wide ebullition dynamics may be modeled without resolving the fine-scale spatial structure of venting.

1. Introduction

Emissions from submerged sediments in lakes, rivers, wetlands, and oceans contribute to atmospheric methane, but the nature and magnitude of the release remain uncertain. Owing to their buoyancy and high methane content, bubbles emitted from the sediment transport methane more efficiently than waters containing dissolved methane, and field studies suggest that ebullition is often the dominant mode of methane transfer to the atmosphere [*Martens and val Klump*, 1980; *Kuipphet and Martens*, 1982; *Keller and Stallard*, 1994; *Bastviken et al.*, 2004; *Walter et al.*, 2006; *Bastviken et al.*, 2011; *Maeck et al.*, 2013a]. Ebullitive emissions are episodic and spatially heterogeneous, which complicates upscaling of flux estimates [*Greinert*, 2008; *Ostrovsky et al.*, 2008; *Greinert et al.*, 2010; *DelSontro et al.*, 2011; *Wik et al.*, 2011; *Maeck et al.*, 2013b; *Walter Anthony and Anthony*, 2013; *Wik et al.*, 2013; *DelSontro et al.*, 2015].

The episodicity of methane venting may be driven by either the methane source or an external forcing, depending on which operates on a faster time scale [*Maeck et al.*, 2013b]. For example, drops in hydrostatic or atmospheric pressure trigger ebullition from methane-generating lake sediments [*Scandella et al.*, 2011] and marine sediments [*Martens and val Klump*, 1980; *Kuipphet and Martens*, 1982; *Chanton et al.*, 1989], possibly even in the presence of methane hydrates [*Torres et al.*, 2002]. Spatial heterogeneity in methane venting often manifests as hyperactive vents or vent clusters, sometimes referred to as hot spots [*Walter et al.*, 2006; *Wik et al.*, 2011; *DelSontro et al.*, 2015]. These focused release points may be associated with enhanced microbial methanogenesis [*Ostrovsky et al.*, 2008; *DelSontro et al.*, 2011; *Maeck et al.*, 2013a; *Wik et al.*, 2013], sediment morphological features like pockmarks [*Bussmann et al.*, 2011], a geologic source [*Walter Anthony et al.*, 2012], dissociating gas hydrates [*Westbrook et al.*, 2009; *Berndt et al.*, 2014; *Skarke et al.*, 2014], or rapidly degrading permafrost [*Shakhova et al.*, 2014]. The persistence of bubble outlets and the spacing and variability between them can potentially be used to distinguish the mechanisms controlling ebullition [*Greinert*, 2008; *Wik et al.*, 2011], but observations of these critical parameters are sparse and inconclusive.

Ebullitive fluxes are sometimes measured using bubble traps deployed at discrete locations over an extended time period, but capturing hot spot ebullition or the episodicity of venting events can be challenging with this approach [*Walter et al.*, 2006; *Varadharajan and Hemond*, 2012; *Maeck et al.*, 2013b; *Walter Anthony and Anthony*, 2013; *Wik et al.*, 2013]. Hydroacoustic surveys from ships [*Ostrovsky et al.*, 2008; *Greinert et al.*, 2010;
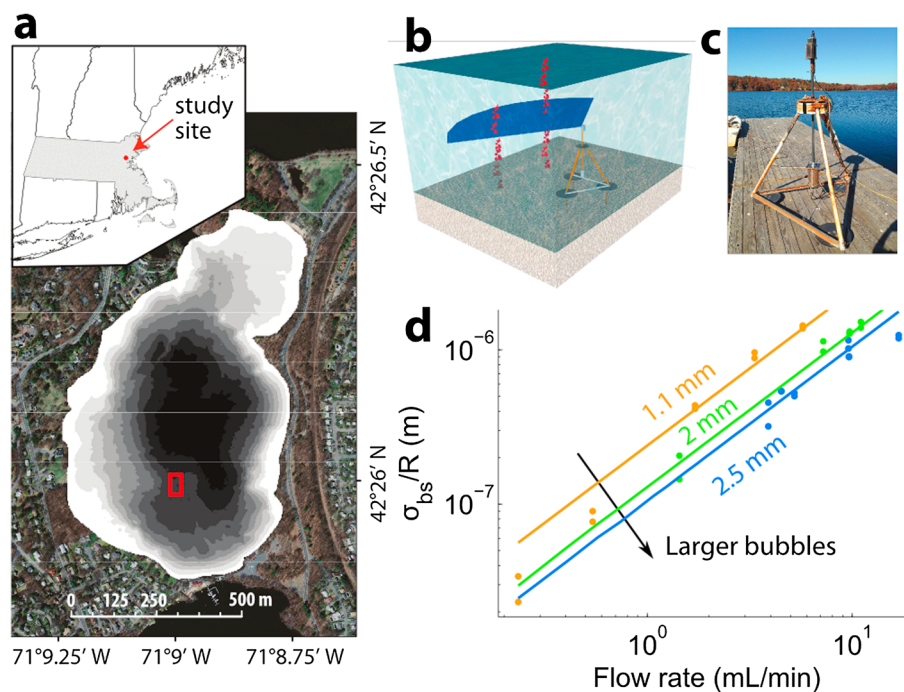
Figure 1. Study area, sonar lander, and calibration. (a) Location of Upper Mystic Lake (inset, Massachusetts, USA shaded) and bathymetry at 2.5 m shaded intervals superposed on an aerial photomosaic. Red square indicates the region bounding the deployment locations (see supporting information). (b) Diagram showing streams of bubbles (red) rising through the horizontally oriented multibeam sonar fan (blue, not to scale). (c) Photo of the deployment tripod before redeployment. (d) Calibration curves over 2 orders of magnitude in gas flow rate and for three different bubble size classes. Data points represent the time-averaged sonar response to streams of a given flow rate, and lines indicate modeled responses for each bubble class (radius in millimeter, see supporting information).

DelSontro et al., 2011, 2015; *Skarke et al.*, 2014; *Weber et al.*, 2014] cover large areas but only at discrete times and therefore cannot be used for continuously quantifying fluxes. Short- and long-term seafloor deployments of hydroacoustic sensors [*Greinert*, 2008] can detect ebullitive events at specific locations but require careful calibration to infer spatially resolved fluxes. Here we extend the hydroacoustic approach to acquire long-term, high-resolution methane emission records from a lake bottom to test hypotheses about the driving forces for ebullition events and the mechanisms controlling spacing and persistence of gas vents.

2. Multibeam Sonar Deployment

An Imagenex 837B DeltaT 260 kHz rotating multibeam sonar was deployed on a benthic lander in the deep-water basin (18–19 m) of Upper Mystic Lake (UML), an eutrophic kettle lake north of Boston, MA (Figure 1). The sonar surveyed in a horizontal plane ≈1.5 m above the lake's bottom and ≈8–9 m below the depth of observed thermoclines to collect data over a 9 month period in a ≈330 m^2 area. The sediments within this region are organic rich (20–40%) [*Spliethoff and Hemond*, 1996] and remain anoxic and at roughly constant temperature beneath the 4–6°C hypolimnetic water [*Varadharajan*, 2009]. The previously measured sediment accumulation rate of 0.5 cm/yr is expected to be homogeneous within the basin due to relatively flat bathymetry, and freeze cores from within the basin show strikingly similar depth profiles of arsenic concentration [*Spliethoff and Hemond*, 1996]. Over the scale of the lake, deposition rates are expected to be faster near the periphery and the northern end, where water flows in from a forebay. An identical sonar was calibrated in a 1300 m^3 freshwater tank at the University of New Hampshire to convert the sonar signals into estimates of the instantaneous flow rate from bubble streams (Figure 1d), which were then integrated to calculate the flux associated with ebullition episodes (see Methods and supporting information).

3. Temporal Signature of Methane Venting

Episodicity observed in spatially averaged daily flux from the sonar data confirms that strong venting episodes can be triggered by drops in hydrostatic pressure (Figure 2a), although the negative correlation of ebullition
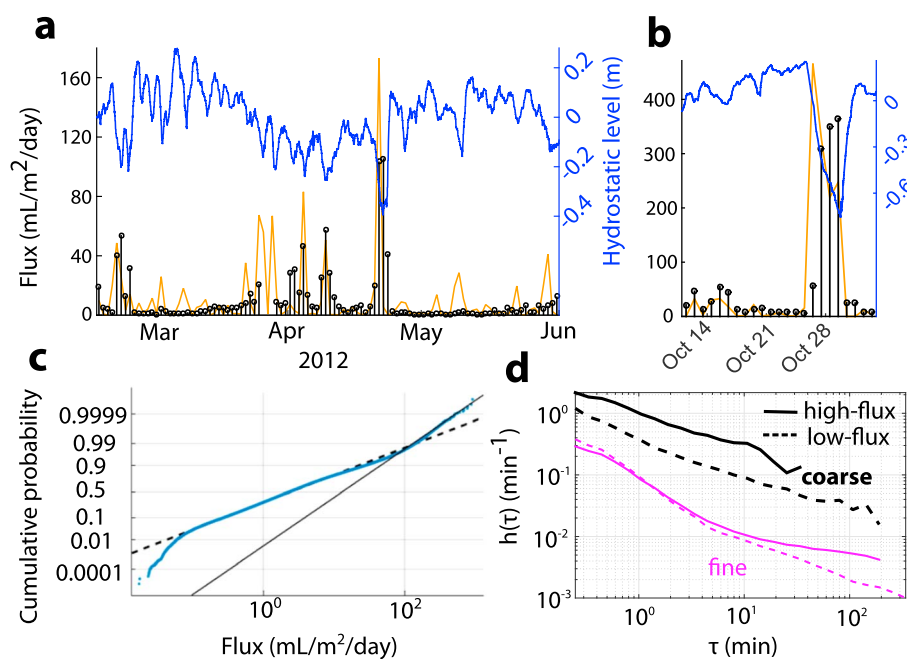
Figure 2. Episodicity of methane venting. (a) Time series of daily, spatially averaged fluxes (black bars) from 10 February through 31 May 2012 shows that enhanced fluxes are triggered by hydrostatic pressure drops (blue line). The episodicity of this triggering can be reproduced using a mechanistic numerical model of gas release through dynamic conduits (orange line). (b) Time series from October 2012, when a hydrostatic pressure drop of 1 m beginning on 26 October triggered massive venting (note the different axis scales) at a different location from the data presented in Figure 2a (see supporting information). (c) Cumulative distribution of 1 min spatially averaged flux values shows three distinct lognormal regimes, which each appears as lines of constant slope on the given axes. (d) The hazard function h decays as a power law with interarrival time τ for coarse (64 m^2, black) and fine (0.25 m^2, red) pixels during high-flux (solid lines) and low-flux (dashed lines) periods.

rate with hydrostatic pressure and its rate of change ($R^2 = 0.5$ and 0.1, respectively) is weak, primarily because not all hydrostatic pressure drops trigger ebullition episodes. For example, the releases in late February and late April 2012 are both followed by month-long periods of relative quiescence, despite several ≈ 0.3 m hydrostatic drops that had earlier been enough to trigger large methane releases. The duration of these quiescent periods reflects the time for sediments to recharge the trapped bubbles to a size large enough to be susceptible to mobilization by hydrostatic triggering.

Hydrostatic triggering of ebullition may be explained mechanistically as a response to changes in effective stress. With falling hydrostatic pressure, total stress is reduced, forcing gas-charged sediments into a more tensile effective stress state. At a critical stress, gas-filled cavities then dilate near-vertical conduits to the sediment's surface [*Boudreau et al.*, 2005; *Jain and Juanes*, 2009], and the critical stress may be modeled assuming that the sediment-water matrix is elastic [*Algar et al.*, 2011a, 2011b] or plastic [*Scandella et al.*, 2011]. The timing and relative magnitude of many of the peak ebullition events can be reproduced using a numerical model [*Scandella et al.*, 2011] that captures this process and that is tuned with another UML data set (Figures 2a and 2b). The tuning parameter, the ebullition number, controls the episodicity of methane fluxes and reflects the balance between the tensile strength of the sediment-water matrix and the characteristic hydrostatic pressure variations. The model can capture the features of most large ebullition events, although it does not fully reproduce the long quiescent periods during March and May 2012 (Figures 2a and 2b).

The high temporal resolution, together with the large areal coverage and long duration of the sonar record, allows for a more detailed analysis of ebullition dynamics that had previously been possible with bubble-trap methods. High-frequency flux measurements (binned at 1 min) show that approximately 98% of the flux measurements follow a lognormal distribution over 3 orders of magnitude (0.1 – 100 mL/m^2/d) (Figure 2c, see supporting information). Lognormally distributed measurements typically arise from processes controlled by the product of independent factors, which in this setting may include the bubble mobilization rate over the observation area and heterogeneity in conductivity of dynamic gas escape pathways.

Further insight into processes controlling ebullition is furnished by the distribution of interarrival times between bubble-release events—"events" are bubble-release sequences that persist with breaks no longer than 2 s (given 5 s moving-average filtering). Distributions of interarrival times may be analyzed using the hazard function

$$h(\tau) = \frac{f(\tau)}{1 - F(\tau)}, \tag{1}$$

where $f(\tau)$ is the probability density function of interarrival times τ, and $F(\tau)$ is the cumulative density function [*Stapelberg*, 2009]. $h(\tau)$ quantifies the probability of an event occurring conditioned on a given amount of time having passed since the last event. For a Poisson process, events are independent and have uniform probability, corresponding to constant h since the events have no memory of previous arrivals. For a Weibull process—a model often used in reliability engineering to model component failures—the hazard function is a power law, $h(\tau) = (\beta/\lambda)(\tau/\lambda)^{\beta-1}$, where β and λ are the shape and scale parameters, respectively. A decreasing power law ($\beta < 1$) corresponds to strong temporal clustering, while an increasing power law ($\beta > 1$) is associated with more regularly periodic arrivals [*Stapelberg*, 2009].

In UML, ebullition events are characterized by decaying power laws. For events collected from a 64 m² averaging area, the decay in both high- and low-flux regimes is well fit by $\beta \approx 0.4$, which reflects mild temporal clustering (Figure 2d). At the fine-scale resolution of the sonar (0.25 m²), $h(\tau)$ shows two distinct regimes characterized by different power law scalings. For short-term interarrival times ($\tau < 5$ min), the decay has a slope less than -1, indicating stronger short-term clustering than possible with a Weibull process, which requires $\beta > 0$. The power law regime does not extend over all τ but instead transitions to a regime of more gradual decay over long interarrival times ($\tau > 5$ min), consistent with reestablishment of sediment cohesion and healing of vent conduits. Over long τ, the high-flux regime shows even more gradual decay in $h(\tau)$ than the low-flux regime, implying a larger role for independent arrivals.

4. Spatial Signature of Methane Venting

The spatial structure of methane venting is found to depend on the overall flux regime (high flux versus low flux). Daily gas flux maps during high-flux periods reveal gas release from densely spaced outlets, while the low-flux periods are associated with sparser venting (Figure 3a). The ubiquity of venting across the observation area during high-flux periods may reflect the relative homogeneity of methanogenesis, whose controlling parameters (sediment accumulation and temperature) are fairly homogeneous above the meter scale in the deepwater basin [*Spliethoff and Hemond*, 1996].

During high-flux periods, ebullition events occur in clusters of enhanced activity, although, over time, events appear throughout the field of observation. While some locations vent gas at over 3 times the spatiotemporal mean flux of 10 mL/m²/d (Figure 3b), these contribute only 1% of the total flux, suggesting a minimal role for hot spots. Instead, gas appears to be released through independent, near-vertical conduits or conduit networks linked to outlets, where the scale of lateral transport or significant heterogeneity in sediment properties is less than the resolution of the sonar, 0.5 m. Such a laterally dense network of release pathways should develop in sediments that generate methane throughout their bulk. In this case, transport from the sediment matrix toward release pathways would be diffusion limited to a distance on the scale of centimeters in the days to weeks between ebullition events. The outlet and conduit spacing may also be controlled by heterogeneity in the chemistry and mechanics of the sediments, though our results show that such heterogeneity does not give rise to persistent outlets spaced more than 0.5 m apart.

A spatial clustering analysis of the observed methane-flux signal yields additional clues about the system's self-organization. Our analysis is based on the radial distribution function (RDF), $g(r)$, which detects clustering as a function of interpoint distance r [*Illian et al.*, 2008] (see Methods and supporting information). The analysis yields $g > 1$ for short-range ($r < 1$ m) events over short time periods (10 min and 1 h samples), indicating a high areal density of events relative to a completely spatially random (CSR) process. The short-range clustering is balanced by long-range spacing ($g < 1$ for $r > 1$ m). This signature of short-range clustering and long-range spacing was strongest for 10 min samples and became progressively weaker for longer duration samples, eventually decaying to a homogeneous RDF ($g(r) \approx 1$) over daily samples (Figure 3d). This clustering signature indicates that gas is vented from nearby, distinct outlets within a short period of time (see Methods and supporting information).
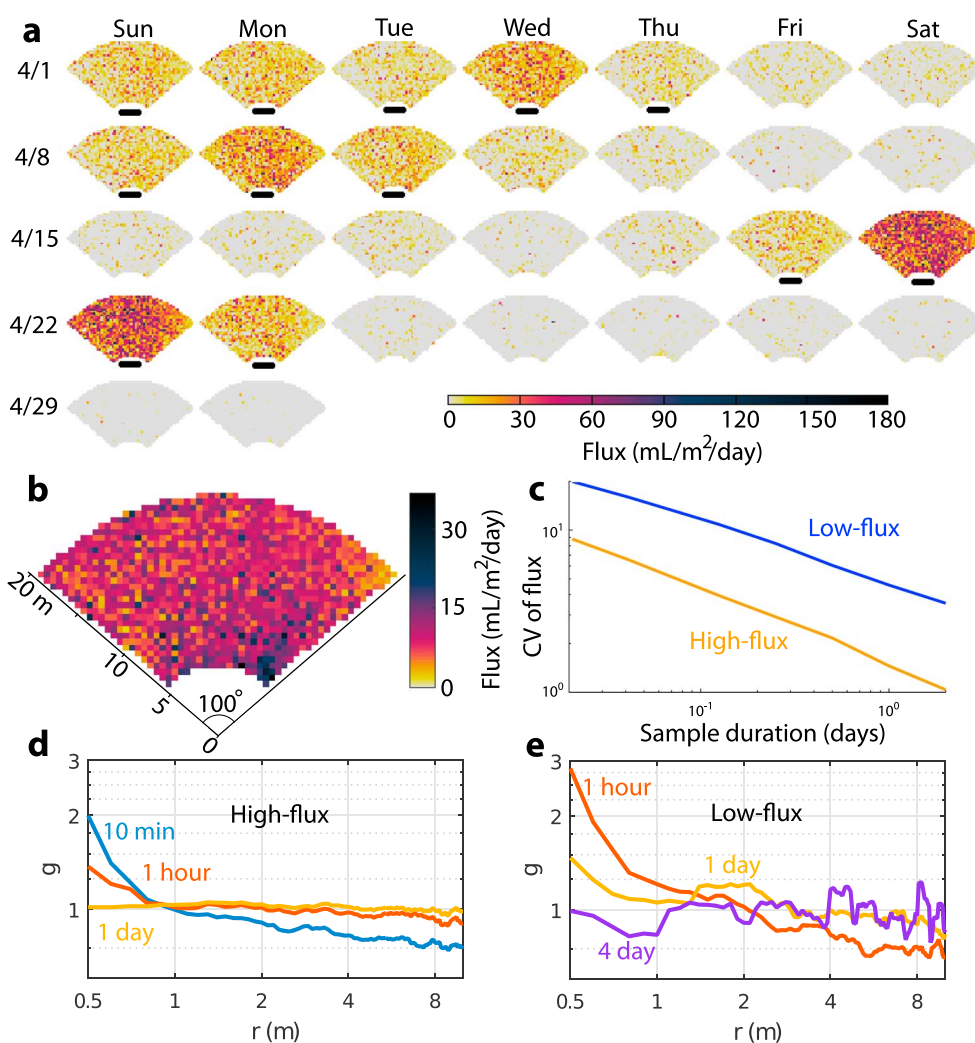
Figure 3. Spatial structure of methane venting. (a) This calendar representation of daily sonar-detected gas venting in April 2012 shows the spatial variability of methane fluxes across the sonar detection area. Days with higher than average flux are underlined. (b) Average flux map from March to May 2012. (c) Spatial coefficient of variation (CV) between flux measurements on a grid with resolution of 0.5 m, averaged over samples of duration 1–24 h collected during Spring 2012. (d and e) Radial distribution function (RDF), $g(r)$, for high-flux (Figure 3d) and low-flux (Figure 3e) periods during Spring 2012.

Compared with the high-flux regime, low-flux periods show both stronger variability and longer persistence in the structure of the heterogeneity. For a given observation duration, the coefficient of variation (CV) across space is more than twice the CV from high-flux periods (Figure 3c). The spatial structure of this variability is evident in the RDF, which exhibits short-range spatial clustering that is similar to the clustering observed during high-flux periods, except that it extends to $r \leq 2$ m and persists over timescales as long as 1 day (Figure 3e, see supporting information).

The ephemeral nature of spatial clustering evidenced by the RDF is consistent with the spatial localization of short-term temporal clustering observed in $h(\tau)$ and is likely associated with the same process. Ebullition events may trigger "aftershock" events by mechanically disturbing nearby sediments that contain critically stressed gas pockets. Due to the compliance of the sediments and the small magnitude of deformation associated with bubble passage, this mechanism would likely require that trapped bubbles be spaced only a few centimeters apart.

The decay of clustering over progressively longer periods indicates that individual outlet clusters are active for a short time but do not persist to dominate the long-term flux pattern. Instead, independent outlets or clusters subsequently become active at intermediate, independent locations until the domain is filled with

emission sites approximating a CSR pattern. The clustering pattern in the RDF decays faster during high-flux periods, suggesting that higher fluxes arise primarily from more frequent initiation of spatially independent events. The spatial independence of new arrivals over long time periods is consistent with the conceptual model that long-term, large-scale fluxes are driven by hydrostatic pressure drops, which act equally over the sediment surface to liberate trapped gas.

5. Conclusions

In summary, the high spatial and temporal resolution afforded by the sonar data allows discernment of discrete ebullitive episodes and vent locations, and the long deployments permit analyses over months' long periods. Our analysis shows that specific methane vents in UML do not repeatedly dominate fluxes during ebullitive episodes; instead, vents are frequently forming and closing off throughout the homogeneous sediments that make up the seep field in the lake's deep basin. This finding challenges the idea that sediment vents, once established, will continue to be the preferential loci over the scale of meters. While these results may not directly apply to settings with more heterogeneous geology [*Hornbach et al.*, 2004; *Walter Anthony et al.*, 2012; *Skarke et al.*, 2014] or sediment deposition patterns [*Bussmann et al.*, 2011; *DelSontro et al.*, 2011; *Maeck et al.*, 2013a; *DelSontro et al.*, 2015], they suggest that the acquisition of longer and more spatially comprehensive data sets on ebullition events in such settings may better constrain the relative importance of hot spot versus distributed methane emissions from submerged sediments for both local and global flux estimates.

Appendix A: Methods Summary

A1. Sonar

The sonar data were acquired using an Imagenex 837B multibeam profiling sonar, which detects acoustic targets with high spatial and temporal resolution over a roughly planar observation area, a fan of ≈100° by ≈2°. The pulse repetition rate was approximately 6 Hz so that bubbles at 1 and 20 m range were insonified by 1 and 30 consecutive pings, respectively. The locations of the detected bubbles are accurate to < 0.5 m because the distance resolution was 0.18 m and the angular resolution of 1° corresponds to at most 0.4 m at the maximum range of 20 m. The horizontal orientation of the unit was set using a gimbal and measured to remain within ≈0.2° of horizontal with an on-board pitch-roll-heading sensor.

The directional sensitivity of the sonar was corrected using a combination of the beam pattern measured in the ocean engineering tank at the University of New Hampshire (UNH) and tuning to remove large-scale directional sensitivity from the long-term average flux during a given multimonth deployment period (see supporting information).

A2. Calibration

The sonar was calibrated to estimate the volumetric flow rate of bubble streams rising through its observation area of ≈330 m². The calibration was performed on a unit of the same model in the Ocean Engineering tank at UNH by injecting bubbles at a constant flow rate and bubble size distribution from beneath the sonar fan. The bubble sizes were measured independently using a camera in a waterproof housing, and the rate of bubble release was monitored with a passive hydrophone. The time-averaged backscatter $\overline{\sigma}_{bs}$ measured by the sonar scaled linearly with the flow rate Q at a given bubble size, and the calibration coefficient K varied with the bubble size (Figure 1d),

$$Q = K \left(\frac{\overline{\sigma}_{bs}}{R} \right),$$ (A1)

where R is the range, the distance from the sonar head to the target. The dependence on flow rate and bubble size matched predictions from an analytical model of the expected sonar response to a constant bubble stream rising through a horizontally oriented multibeam sonar. The expected response from a bubble stream with a wide but constant bubble size distribution was calculated by adapting a method that was developed for single and split beam sonar [*Muyakshin and Sauter*, 2010; *Veloso et al.*, 2015], assuming a constant bubble size distribution measured in UML with an optical bubble sizer [*Delwiche et al.*, 2015] and assuming that plumes are too sparse to be influenced significantly by multiple scatter reflections (see supporting information). The relative uncertainty in flux estimates is estimated to be ~70% (see supporting information).

A3. Bubble Identification

After the raw data were smoothed with a 5 s moving-average filter and coarsened to 1 s resolution, they were thresholded to identify connected groups of pixels contributing a minimum flow rate, 0.03 mL/min. Ebullition events, comprising a series of bubbles released in rapid succession from the same location, were identified from the time series of flow rates from these active groups as periods of nonzero activity with breaks of no more than 2 s. The volume of gas estimated by the sonar was adjusted to STP.

Candidate ebullition events were distinguished from nonbubble targets with limits on their intensity and duration, and this process correctly classified >99% of both the bubble and nonbubble volume (see supporting information).

A4. Hazard Function

The hazard function was estimated using a histogram of the event interarrival times to estimate $f(\tau)$, which was then converted to $h(\tau)$ using the definition in equation (1). Logarithmically spaced bins were used to reduce the variance of the estimator at long interarrival times, and the estimator was validated with simulations of Poisson and Weibull processes. A minimum interarrival time of 15 s was used because this represents the characteristic duration of bubbling events. In order to analyze long, continuous records in each location, day-long samples were classified as either high flux or low flux based on their relation to the long-term average flux, which is independent of the time scale of coarsening.

A5. Radial Distribution Function

To account for the enhanced importance of events releasing large volumes of gas, the volume-weighted RDF $g(r)$ was estimated using the marked pair correlation function [*Illian et al.*, 2008] (see supporting information). Estimating the RDF requires an observation window within which the data are first-order stationary in density and magnitude [*Illian et al.*, 2008]. This stationary window was found to span the central 60° of the sonar fan and from 6 to 20 m from the sonar head (Figure 3b), after correcting for the directional sensitivity of the sonar.

A6. Conduit Dilation Model

The episodicity of spatially-averaged fluxes was reproduced with a numerical, mechanistic model of methane gas transport through dynamic conduits that dilate in response to changes in effective stress [*Scandella et al.*, 2011]. This 1-D model captures the accumulation of trapped gas in a vertical column of sediment and tracks the gas pressure and volume as a hydrostatic pressure forcing triggers plastic deformation of the sediment-water matrix surrounding gas cavities. When the effective stress reaches a depth-dependent tensile strength threshold, the gas forces open a conduit to the surface and escape. The fundamental parameter of the model, called the ebullition number, N_e, reflects the balance between the vertical gradient in tensile strength of the mud and the characteristic magnitude of hydrostatic pressure changes. Larger values of N_e require larger, rarer drops in hydrostatic pressure to release gas from the deepest sediments and thus drive more strongly episodic venting. In this study, the best fit value of $N_e = 5$ was the same as in a previous study on UML that quantified ebullition with floating bubble traps [*Scandella et al.*, 2011].

References

Algar, C. K., B. P. Boudreau, and M. A. Barry (2011a), Initial rise of bubbles in cohesive sediments by a process of viscoelastic fracture, *J. Geophys. Res.*, *116*, B04207, doi:10.1029/2010JB008133.
Algar, C. K., B. P. Boudreau, and M. A. Barry (2011b), Release of multiple bubbles from cohesive sediments, *Geophys. Res. Lett.*, *38*, L08606, doi:10.1029/2011GL046870.
Bastviken, D., J. Cole, M. Pace, and L. Tranvik (2004), Methane emissions from lakes: Dependence of lake characteristics, two regional assessments, and a global estimate, *Global Biogeochem. Cycles*, *18*, GB4009, doi:10.1029/2004GB002238.
Bastviken, D., L. J. Tranvik, J. A. Downing, P. M. Crill, and A. Enrich-Prast (2011), Freshwater methane emissions offset the continental carbon sink, *Science*, *331*, 50.
Berndt, C., et al. (2014), Temporal constraints on hydrate-controlled methane seepage off Svalbard, *Science*, *343*(6168), 284–287.
Boudreau, B., C. Algar, B. Johnson, I. Croudace, A. Reed, Y. Furukawa, K. Dorgan, P. Jumars, A. Grader, and B. Gardiner (2005), Bubble growth and rise in soft sediments, *Geology*, *33*(6), 517–520.
Bussmann, I., S. Schlomer, M. Schluter, and M. Wessels (2011), Active pockmarks in a large lake (Lake Constance, Germany): Effects on methane distribution and turnover in the sediment, *Limnol. Oceanogr.*, *56*(1), 379–393.
Chanton, J., C. Martens, and C. Kelley (1989), Gas transport from methane-saturated, tidal freshwater and wetland sediments, *Limnol. Oceanogr.*, *34*(5), 807–819.
DelSontro, T., M. J. Kunz, T. Kempter, A. Wueest, B. Wehrli, and D. B. Senn (2011), Spatial heterogeneity of methane ebullition in a large tropical reservoir, *Environ. Sci. Technol.*, *45*(23), 9866–9873.
DelSontro, T., D. F. McGinnis, B. Wehrli, and I. Ostrovsky (2015), Size does matter: Importance of large bubbles and small-scale hot spots for methane transport, *Environ. Sci. Technol.*, *49*(3), 1268–1276.
Delwiche, K., S. Senft-Grupp, and H. Hemond (2015), A novel optical sensor designed to measure methane bubble sizes in situ, *Limnol. Oceanogr.*, *13*, 712.

Greinert, J. (2008), Monitoring temporal variability of bubble release at seeps: The hydroacoustic swath system GasQuant, *J. Geophys. Res.*, *113*, C07048, doi:10.1029/2007JC004704.

Greinert, J., D. F. McGinnis, L. Naudts, P. Linke, and M. De Batist (2010), Atmospheric methane flux from bubbling seeps: Spatially extrapolated quantification from a Black Sea shelf area, *J. Geophys. Res.*, *115*, C01002, doi:10.1029/2009JC005381.

Hornbach, M., D. Saffer, and W. Holbrook (2004), Critically pressured free-gas reservoirs below gas-hydrate provinces, *Nature*, *427*(6970), 142–144.

Illian, J., A. Penttinen, H. Stoyan, and D. Stoyan (2008), *Statistical Analysis and Modelling of Spatial Point Patterns*, Wiley, West Sussex, England.

Jain, A. K., and R. Juanes (2009), Preferential mode of gas invasion in sediments: Grain-scale mechanistic model of coupled multiphase fluid flow and sediment mechanics, *J. Geophys. Res.*, *114*, B08101, doi:10.1029/2008JB006002.

Keller, M., and R. Stallard (1994), Methane emission by bubbling from Gatun Lake, Panama, *J. Geophys. Res.*, *99*(D4), 8307–8319.

Kuipphet, G., and C. Martens (1982), Biogeochemical cycling in an organic-rich coastal marine basin. 3. Dissolved gas transport in methane-saturated sediments, *Geochim. Cosmochim. Acta*, *46*(11), 2049–2060.

Maeck, A., T. DelSontro, D. F. McGinnis, H. Fischer, S. Flury, M. Schmidt, P. Fietzek, and A. Lorke (2013a), Sediment trapping by dams creates methane emission hot spots, *Environ. Sci. Technol.*, *47*(15), 8130–8137.

Maeck, A., H. Hofmann, and A. Lorke (2013b), Pumping methane out of aquatic sediments; forcing mechanisms that affect the temporal dynamics of ebullition, *Biogeosci. Discuss.*, *10*(11), 18,687–18,722.

Martens, C., and J. val Klump (1980), Biogeochemical cycling in an organic-rich coastal marine basin. 1. Methane sediment-water exchange processes, *Geochim. Cosmochim. Acta*, *44*(3), 471–490.

Muyakshin, S. I., and E. Sauter (2010), The hydroacoustic method for the quantification of the gas flux from a submersed bubble plume, *Oceanology*, *50*(6), 1045–1051.

Ostrovsky, I., D. F. McGinnis, L. Lapidus, and W. Eckert (2008), Quantifying gas ebullition with echosounder: The role of methane transport by bubbles in a medium-sized lake, *Limnol. Oceanogr.*, *6*, 105–118.

Scandella, B. P., C. Varadharajan, H. F. Hemond, C. Ruppel, and R. Juanes (2011), A conduit dilation model of methane venting from lake sediments, *Geophys. Res. Lett.*, *38*, L06408, doi:10.1029/2011GL046768.

Shakhova, N., et al. (2014), Ebullition and storm-induced methane release from the East Siberian Arctic Shelf, *Nat. Geosci.*, *7*(1), 64–70.

Skarke, A. D., C. D. Ruppel, M. Kodis, D. Brothers, and E. Lobecker (2014), Widespread methane leakage from the sea floor on the northern US Atlantic margin, *Nat. Geosci.*, *7*(9), 657–661.

Spliethoff, H., and H. Hemond (1996), History of toxic metal discharge to surface waters of the Aberjona Watershed, *Environ. Sci. Technol.*, *30*(1), 121–128.

Stapelberg, R. F. (2009), *Handbook of Reliability, Availability, Maintainability and Safety in Engineering Design*, Springer, London.

Torres, M., J. McManus, D. Hammond, M. de Angelis, K. Heeschen, S. Colbert, M. Tryon, K. Brown, and E. Suess (2002), Fluid and chemical fluxes in and out of sediments hosting methane hydrate deposits on Hydrate Ridge, OR, I: Hydrological provinces, *Earth Planet. Sci. Lett.*, *201*(3–4), 525–540.

Varadharajan, C. (2009), Magnitude and spatio-temporal variability of methane emissions from a eutrophic freshwater lake, PhD Thesis, Massachusetts Inst. of Technol., Cambridge, Mass.

Varadharajan, C., and H. F. Hemond (2012), Time-series analysis of high-resolution ebullition fluxes from a stratified, freshwater lake, *J. Geophys. Res.*, *117*, G02004.

Veloso, M., J. Greinert, J. Mienert, and M. De Batist (2015), A new methodology for quantifying bubble flow rates in deep water using splitbeam echosounders: Examples from the Arctic offshore NW-Svalbard, *Limnol. Oceanogr. Methods*, *13*(6), 267–287.

Walter, K. M., S. A. Zimov, J. P. Chanton, D. Verbyla, and F. S. Chapin III (2006), Methane bubbling from Siberian thaw lakes as a positive feedback to climate warming, *Nature*, *443*, 71–75.

Walter Anthony, K. M., and P. Anthony (2013), Constraining spatial variability of methane ebullition seeps in thermokarst lakes using point process models, *J. Geophys. Res.*, *118*(3), 1015–1034.

Walter Anthony, K. M., P. Anthony, G. Grosse, and J. Chanton (2012), Geologic methane seeps along boundaries of Arctic permafrost thaw and melting glaciers, *Nat. Geosci.*, *5*, 419–426.

Weber, T. C., L. Mayer, K. Jerram, J. Beaudoin, Y. Rzhanov, and D. Lovalvo (2014), Acoustic estimates of methane gas flux from the seabed in a 6000 km^2 region in the Northern Gulf of Mexico, *Geochem. Geophys. Geosyst.*, *15*(5), 1911–1925.

Westbrook, G. K., et al. (2009), Escape of methane gas from the seabed along the West Spitsbergen continental margin, *Geophys. Res. Lett.*, *36*, L15608, doi:10.1029/2009GL039191.

Wik, M., P. M. Crill, D. Bastviken, A. Danielsson, and E. Norback (2011), Bubbles trapped in arctic lake ice: Potential implications for methane emissions, *J. Geophys. Res.*, *116*, G03044, doi:10.1029/2011JG001761.

Wik, M., P. M. Crill, R. K. Varner, and D. Bastviken (2013), Multiyear measurements of ebullitive methane flux from three subarctic lakes, *J. Geophys. Res. Biogeosci.*, *118*, 1307–1321, doi:10.1002/jgrg.20103.

Supporting Information for
Ephemerality of discrete methane vents in lake sediments

Benjamin P. Scandella[1], Liam Pillsbury[2], Thomas Weber[2],
Carolyn Ruppel[3], Harold F. Hemond[1], Ruben Juanes[1,*]

[1] Department of Civil and Environmental Engineering, Massachusetts Institute of Technology
[2] Department of Mechanical Engineering, University of New Hampshire
[3] US Geological Survey, Woods Hole, Massachusetts, USA.

[*]E-mail: juanes@mit.edu

Contents

1 Deployment locations

The data presented in this paper were collected from 2 nearby locations in the deepwater central basin of UML. Their relative locations and deployment periods in 2012 are mapped in Fig. S1.
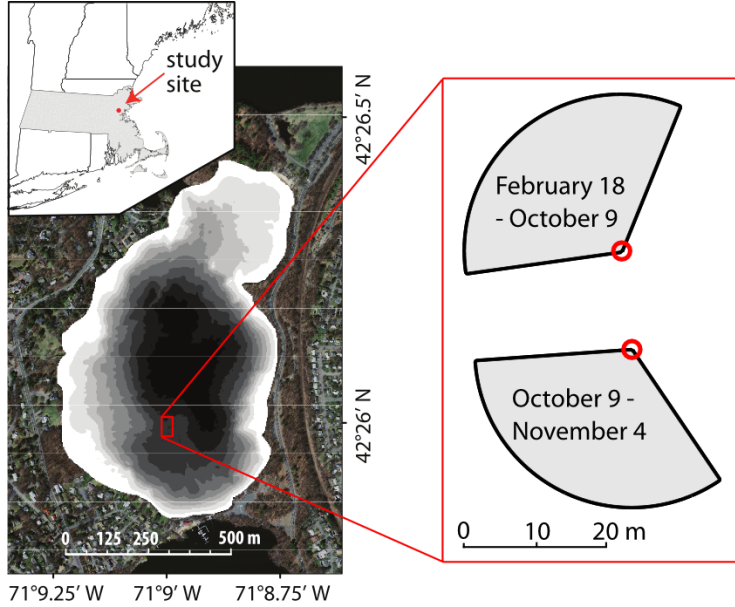

Figure S1: Map showing the relative locations and orientations of the 2 deployment locations where the data presented here were collected.

2 Flux estimation methods

2.1 Backscatter measurement using the Imagenex 837B

The Imagenex 837B Delta T multibeam profiling sonar does not measure backscatter cross-section directly, so we present here the method used to calibrate it for that purpose.

The pressure wave amplitude of the sound received by a sonar unit is that of the source, diminished by spherical spreading and attenuation, and increased by the magnitude of the target causing the reflection. The received amplitude P_{rec} after travel to and from targets with backscatter cross-section σ_{bs} at distance R, with spherical spreading, is:

$$\left(\frac{P_{rec}}{P_0}\right)^2 = \left(\frac{P_{src}(\theta)}{P_0}\right)^2 \left(\frac{R}{R_0}\right)^{-4} 10^{-\frac{2\alpha R}{10}} \frac{\sigma_{bs}}{R_0^2}, \tag{S1}$$

where $P_{src}(\theta)$ is the directionally-dependent amplitude of the source signal, P_0 and R_0 are reference pressure and length values, and α is a coefficient of acoustic attenuation in the water. The use of reference values facilitates handling the sonar equation in logarithmic form, though for the sake of clarity we will use SI units.

The Imagenex DeltaT reports an amplitude that is proportional to the received pressure in each pixel (beam for direction and sample for distance from the sonar head):

$$(a_{\Delta T})^2 \;=\; \left(k_a \frac{P_{rec}(\theta)}{P_0}\right)^2 G^2 \left(\frac{R}{R_0}\right)^2 10^{\frac{2\alpha R}{10}}, \tag{S2}$$

$$G \;=\; 10^{\frac{G_s}{20}}\left(\frac{G_d}{100}\right), \tag{S3}$$

where k_a is an unknown proportionality constant and G is the user-defined gain on the signal. The user-defined gain G depends on 2 parameters, the hardware "StartGain" (G_s) and the software "DisplayGain" (G_d) that scales the data into the 8-bit dynamic range. The power of 2 in R/R_0 compensates for part of the geometric spreading and is applied as a time-varying gain (TVG) to the incoming signal. It is appropriate for quantifying the reflectivity of surface targets that extend past the incident area of the sonar pulse (which is proportional to R^2), as is the case for the sediment surface in a bathymetric survey. Since k_a is Imagenex proprietary information, we define $a_{rec} = k_a P_{rec}/P_0$ and $a_{src}(\theta) = k_a P_{src}(\theta)/P_0$. This way, Equations (S1) and (S2) can each be solved for a_{rec}:

$$a_{rec}^2 \;=\; a_{src}^2 \left(\frac{R}{R_0}\right)^{-4} 10^{\frac{-2\alpha R}{10}} \frac{\sigma_{bs}}{R_0^2} \tag{S4}$$

$$\;=\; \left(\frac{a_{\Delta T}}{G}\right)^2 \left(\frac{R}{R_0}\right)^{-2} 10^{\frac{-2\alpha R}{10}}. \tag{S5}$$

Setting these two equal and solving for σ_{bs} yields:

$$\sigma_{bs} = \left(\frac{a_{\Delta T} R}{a_{src}(\theta) G}\right)^2. \tag{S6}$$

For the data reported here, $G_s = 20$ dB and $G_d = 3$ so that $G = 0.3$. The source amplitude $a_{src}(\theta)$ has two components: a base magnitude a_0 and directional dependence, or horizontal beam pattern, $B_h(\theta)$:

$$a_{src}(\theta) = a_0 B_h(\theta). \tag{S7}$$

The horizontal beam pattern was estimated in a two-step process described below. The base magnitude a_0 was then estimated using a standard 38.1 mm diameter tungsten-carbide calibration sphere in situ ($\sigma_{bs} = 1.19 \times 10^{-4}$ m^2 for $f = 260$ kHz). The sphere was raised and lowered through the sonar fan in a variety of locations (θ and R) to get a record of the maximum $a_{\Delta T}$. Equations (S6) and (S7) were then combined to solve for a_0, yielding estimates of $a_0 = (3.2 \pm 0.7) \times 10^5$ for the unit used in this study.

2.2 Backscatter vs. flux for a multibeam sonar

Sonar is an effective tool for detecting gas bubbles in water because the large contrast in acoustic impedance (product of density and speed of sound) causes pressure waves— when emitted at an appropriate frequency—to reflect strongly off the surface of the bubble.

3

However, estimating the volume within gas bubbles that are detected by sonar is challenging because the magnitude of the sonar signal (the backscatter cross-section, σ_{bs}), is roughly proportional to the total cross-sectional area of bubbles facing the sonar, not their volume. If the distribution of bubble sizes varies little compared with the number of bubbles insonified, the backscatter becomes proportional to the total bubble volume, and therefore the flux [1]. This "inverse" method has been demonstrated at marine ebullition sites using downward-looking, single-beam and split-beam echosounders used during ship-based surveys [1–3]. Here we develop an inverse method for estimating gas fluxes using a fixed-location, horizontally-oriented, profiling multibeam sonar.

While multibeam sonars are typically used with the fan oriented vertically for bathymetric profiling, we used the fan in a horizontal orientation to detect bubbles as they rose through it (Fig. 1c in the main text). A profiling multibeam sonar projects a pulse that is roughly planar and fan-shaped, and the received signal is processed to measure σ_{bs} as a function of both the distance from the sonar head (range) and the direction. A bubble stream rising through the sonar fan contributes to σ_{bs} in a spatially-compact collection of connected pixels. Each pixel, in turn, may insonify multiple bubbles because the fan-shaped pulse has a slight vertical extent (2.2° half-power).

The backscattering measured by the sonar may be expressed as an integral over the radius of bubbles and over the vertical dimension, z:

$$\sigma_{bs} = \int \int N(r, z) \sigma_{bs}(r) B_v^2(z) dr dz, \tag{S8}$$

where $N(r, z)$ is the number of bubbles per radial and vertical unit distance, and $\sigma_{bs}(r)$ is the backscatter from a single bubble of radius r, which may modeled assuming a spherical bubble [4]. B_v is the vertical beam pattern that reflects the sensitivity of the multibeam sonar in the alongship direction.

While the vertical position of individual bubbles within the sonar fan cannot be detected by the sonar, the impact of the vertical beam pattern can be accounted for by averaging measurements over a timescale equivalent to the rise time through the sonar fan (0.2-4 s). Over this timescale, the elevation dependence of N may be neglected, so that the integrals may be separated:

$$\overline{\sigma}_{bs} \approx \int B_v^2(z) dz \int N(r) \sigma_{bs}(r) dr \tag{S9}$$

Because the profiling sonar has a relatively tight beam pattern (small ϕ), the relationship $z = R \tan(\phi)$ may be approximated as $z \approx R\phi$. Applying this change of variables:

$$\overline{\sigma}_{bs} \approx R\phi_e \int N(r) \sigma_{bs}(r) dr, \tag{S10}$$

$$\phi_e = \int B_v^2(\phi) d\phi, \tag{S11}$$

where ϕ_e is the equivalent beam angle: the angle equivalent to the vertical extent of the fan if the sensor had no sensitivity dropoff ($B_v = 1$). The vertical beam pattern $B_v^2(\phi)$ was

measured for the Imagenex 837B during calibration to be Gaussian with half-power angle $\phi_0 = 2.2°$ (Fig. S2):

$$B_v^2(\phi) \approx \exp\left[-\ln(2)\left(\frac{\phi}{\phi_0/2}\right)^2\right], \tag{S12}$$

and, thus, the equivalent beam angle takes the form

$$\phi_e \approx \frac{\phi_0}{2}\sqrt{\frac{\pi}{\ln(2)}}. \tag{S13}$$

where the second equation is the solution of Equations (S11) and (S12).
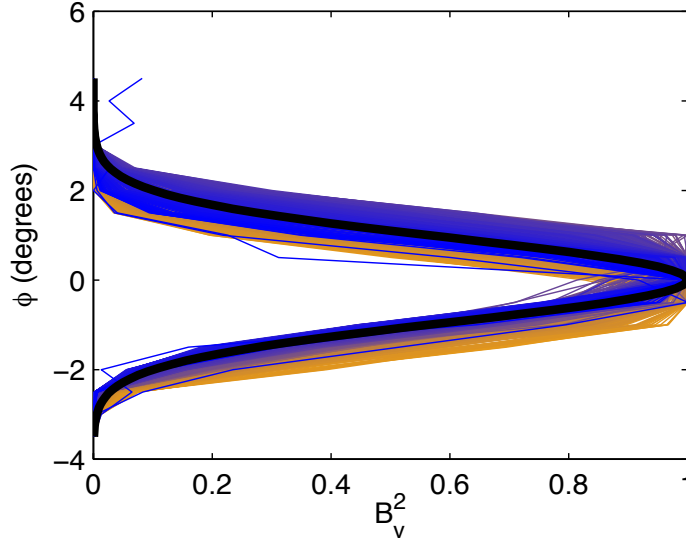

Figure S2: Vertical beam pattern, $B_v(\phi)$, for the Imagenex 837B, as measured in the ocean engineering tank at the UNH (colored lines), and with a Gaussian best-fit curve (black), with half-power angle $\phi_0 = 2.2°$ [Eq. (S12)]. Colors on lines indicate the horizontal (athwartship) beam measured, from $-60°$ (orange) to $60°$ (blue).

The volumetric gas flow rate through a pixel may similarly be expressed as an integral over the bubble radius:

$$Q = \int N(r)V(r)u_{rise}(r)dr, \tag{S14}$$

where u_{rise} is the vertical rise velocity of the bubble, which may be modeled [5], and $V(r) = (4/3)\pi r^3$ is the volume of an assumed-spherical bubble. By combining Equations (S10) and (S14), we obtain:

$$Q \approx \frac{\overline{\sigma}_{bs}}{R\phi_e}\frac{\int N(r)V(r)u_{rise}(r)dr}{\int N(r)\sigma_{bs}(r)dr}. \tag{S15}$$

When the bubble size distribution (BSD), $f(r)$, is relatively constant, the number of bubbles may be expressed as the product of the overall bubble density N_0 and the BSD, $N(r) = N_0 f(r)$. Applying this approximation allows N_0 to cancel from the numerator and denominator, and a combined expression for the flow rate is:

$$Q \approx K \left(\frac{\overline{\sigma}_{bs}}{R} \right), \tag{S16}$$

$$K = \frac{\int f(r) V(r) u_{rise}(r) dr}{\phi_e \int f(r) \sigma_{bs}(r) dr}. \tag{S17}$$

The flow rate estimated by Eq. (S16) is subject to temporal smoothing because $\overline{\sigma}_{bs}$ is measured over a timescale at least equivalent to the time a bubble takes to traverse the sonar fan. This smoothing does not impact estimates of the total volume because the smoothed flow rate is integrated over time. This equation permits theoretical calculation of the coefficient K for an arbitrary BSD. This may be compared with the coefficients used for the inverse method in single-beam and split-beam sonar units [1; 3].

Due to the high spatial resolution of the sonar, bubble streams typically activate a cluster of 2-20 connected pixels, depending on the flow rate and distance from the sonar head. Of interest for our analysis is the total flow rate from a bubble stream, so Eq. (S16) was applied to the sum of connected pixels that were active above a threshold of minimum flow rate:

$$Q_{tot} \approx K' \sum \left(\frac{\overline{\sigma}_{bs}}{R} \right), \tag{S18}$$

$$K' = \frac{K}{f_{overlap}}, \tag{S19}$$

where $f_{overlap}$ is the degree of overlap between neighboring pixels and is measured empirically. As an alternative, one could analyze the maximum backscatter value from within the cluster of pixels, but such a measurement would be more sensitive to the horizontal beam pattern within each beam (Fig. S5) and would neglect the contribution of bubble streams active simultaneously and within a few pixel widths.

Fixed bubble size distribution assumption

The approximation of a constant bubble size distribution (BSD) is most appropriate when the bubble plume is dense enough that the variations in the backscatter derive primarily from changes in the density of bubbles rather than their size. The ebullition events in UML are typically sparse, with only 1-20 bubbles per event, so that variations in the instantaneous backscatter may be primarily due to changes in bubble size and vertical position of the bubbles within the sonar fan. However, the use of 5-second temporal averaging to estimate the flow rate both accounts for the impact of the vertical beam pattern and increases the number of bubbles sampled for a given measurement, making the approximation of constant BSD more appropriate.

Some single-beam and split-beam sonar units independently report both the backscatter cross-section and the distribution of backscattering values from individual bubbles [5; 6] that allow simultaneous estimation of the BSD and flow rate. However, such detail is typically not available from multibeam sonar units like the one used in our study.

Multiple scatter reflections

When multiple nearby bubbles are insonified, the received sonar signal amplitude may be composed of not only the direct backscatter from each of the bubbles, but also the multiple-scatter signal that bounces between multiple bubbles. The relative intensity of a multi-scatter signal depends on the scattering from each target and the distance between them. To estimate the importance of this effect, consider two identical bubbles separated from each other by distance D and from the sonar head by range R. The scattering from a gas bubble may be up to 10 times that of the backscattering for $kr < 10$ [7], so the scattering cross-section from the multi-scatter signal (σ_{multi}) is:

$$\sigma_{multi} \leq \frac{10\sigma_{bs}^2}{4\pi D^2}, \tag{S20}$$

$$\overline{\sigma}_{ms} = \frac{\sigma_{multi}}{\sigma_{bs}} \leq \frac{10\gamma}{4}\left(\frac{r}{D}\right)^2, \tag{S21}$$

where γ is the scattering normalized by the cross-sectional area. For bubbles in the size range of $a \in [0.5, 5]$ mm, $\gamma \approx 0.1$ [7] so that for inter-bubble distance $D > 5$ mm, $\overline{\sigma}_{ms} \leq 10^{-2}$. If $Q = Vu/D$, where V is the bubble volume for bubbles rising in a homogeneous vertical stream, then we can define $\overline{\sigma}_{ms}$ as a function of Q and r:

$$D = \frac{Vu}{Q} = \frac{4ur^3}{3Q}, \tag{S22}$$

$$\overline{\sigma}_{ms} \leq \frac{5\gamma}{2}\left(\frac{3Q}{4\pi ur^2}\right)^2. \tag{S23}$$

This allows us to define iso-lines of $\overline{\sigma}_{ms}$ in the space of Q and r, a lower bound for Q required to make multi-scatter signals detectible at a given tolerance $\overline{\sigma}_{ms}$,

$$Q \geq \sqrt{\frac{2\pi\overline{\sigma}_{ms}}{5\gamma}}\frac{4\pi ur^2}{3}. \tag{S24}$$

Thus, the flow rate threshold at a given tolerance for multi-scatter signals increases with the square of the bubble radius, and high-flow bubble streams with small bubbles are the most conducive to multi-scatter (Fig. S3). For the range of bubble sizes and flow rates observed in the lake, multi-scatter signals are expected to contribute typically less than 1% of the total sonar signal and only rarely up to 10%, so their influence is neglected.

2.3 Calibration experiment

This flux-estimation model was tested during a calibration experiment in the Ocean Engineering Tank at the University of New Hampshire (UNH). Gas was released at constant flow rates from an aperture that produced a fairly narrow range of bubble sizes, which were measured with underwater photographs. The rate of bubble release was measured using a passive hydrophone near the bubble outlet. The time-averaged sonar signal $\overline{\sigma}_{bs}/R$ was summed over all the pixels activated by a given bubble stream, which typically ranged from 2–20 pixels depending on width of the plume and its distance R from the sonar head. This
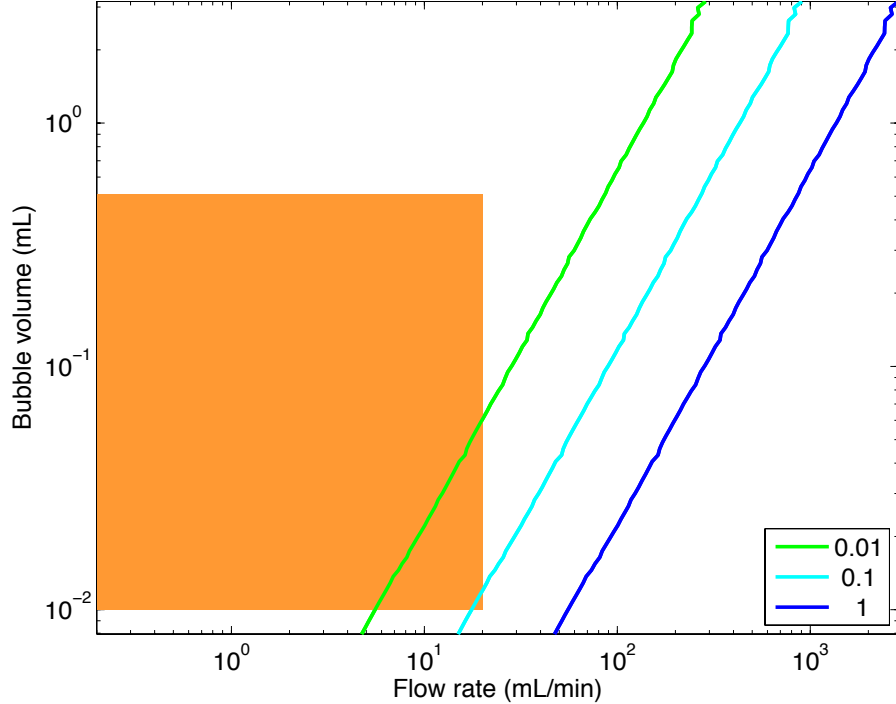
Figure S3: Normalized multiple-scatter reflection magnitude $\overline{\sigma}_{ms}$ (isolines in legend) as a function of flow rate and bubble volume. The shaded orange region shows the range of bubble sizes and flow rates expected to be encountered, from the BSD [8] and from the limits on mean flow rate for distinguishing bubbles from anchor lines. In most cases we expect multi-scatter reflections to contribute less than 1% of the signal, and only above 10% for the cases of highest flow rates with smallest bubbles.

summed sonar signal was plotted against the flow rate for a range of Q (Fig. 1**d** in the main text). These measurements were compared against the modeled response for 3 different bubble size classes ranging from 1.1–2.5 mm in radius. The modeled response fit the data when $f_{overlap} = 1.4$.

Bubble image analysis

In addition to passive acoustic methods, bubble photographs were used to estimate the bubble sizes. The observation area was back lit with a powerful underwater light behind a 1/4-inch translucent plastic diffuser panel. Individual images were taken every second for at least 1 minute during the calibration tests, and the bubbles were identified and sized automatically using MATLAB. Bubbles were identified by a best-fit ellipse on a group of nearby pixels that correspond to edges in intensity in the red channel. Edge pixels were identified using the Canny method, which identifies pixels in a gradient with magnitude above a given threshold. We used lower and upper thresholds of 0.0002 and 0.005, respectively, and a Gaussian filter with width of 1 pixel. Edge pixels were grouped with their neighbors using the density-based scan algorithm [9]. For these pixel groups, best-fit ellipses were identified using MATLAB's `regionprops` function, and the radii were shrunk by 20% to match the

images [10] (Fig. 2.3). Bubble volumes were estimated assuming that the bubbles were oblate spheroids so that $V = \frac{4}{3}\pi r_{max}^2 r_{min}$, where r_{max} and r_{min} are the respective major and minor axes of an ellipse. Bubbles smaller than 0.5 mm in radius were rejected from the automated processing algorithm, to avoid spuriously treating image noise as bubbles.
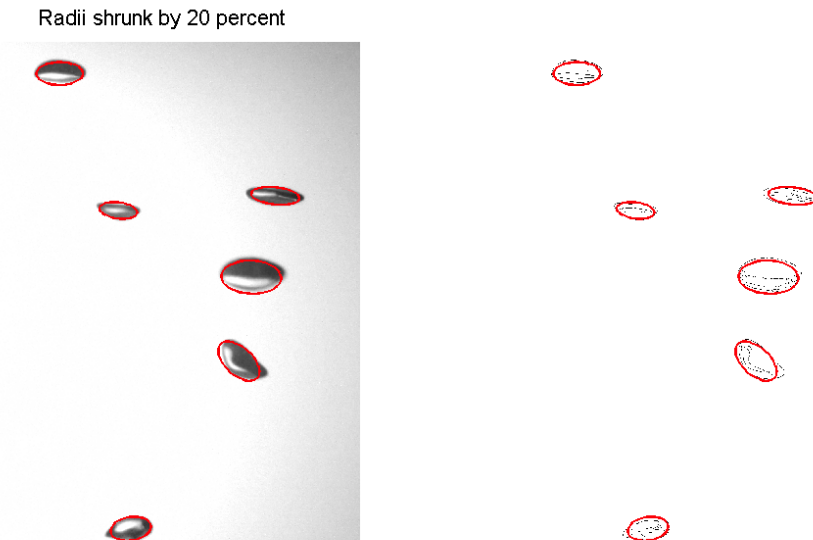

Figure S4: Automatic bubble identification from calibration images. Left: grayscale image with identified ellipses superimposed in red. Right: edge pixels with the same ellipses. In both cases, the radii are reduced by 20% from those identified using MATLAB's `regionprops` tool.

2.4   Classification of events

Events were identified from the sonar data in a way appropriate for detecting and quantifying ebullition, although other targets can manifest themselves as bubble events. The bottom of UML is a fairly quiescent zone, with slow seich-driven current on the order of 5 cm/s and oxygen levels too low to support aerobic biota like fish. However, strong sonar returns were caused by ropes and chains connecting buoys to anchors. These targets can be clearly distinguished from bubbles by their persistence and slow lateral drift, which can be observed directly in animations of the sonar signal. We implemented an automated workflow, which classified the events using thresholds on their duration, total volume released, and intensity (mean and maximum flow rate). The values of these thresholds were chosen to as to achieve high rates of correct identification of both bubbles and anchors.

2.5   Beam pattern

Every sonar unit exhibits directionality dependence in the strength of the sonar returns. To correct for this dependence, we normalized the data with a beam pattern found through a combination of detailed calibration and tuning to eliminate the remaining large-scale pattern.

The beam pattern of an Imagenex 837B sonar unit was measured in the ocean engineering tank at UNH using a 38.1 mm diameter tungsten-carbide calibration sphere, using a rotating pole to turn the sonar head horizontally (athwartship) and a motorized spool and sensor to raise and lower the sphere vertically (alongship). Tests were carried out at 4 and 8 m, though the 8 m test was less reliable due to interactions with the wall in one direction. The high-resolution 4-m test shows a roughly Gaussian shape with a central peak and high-frequency oscillations that correspond to the sensitivity within each beam (Fig. S5).
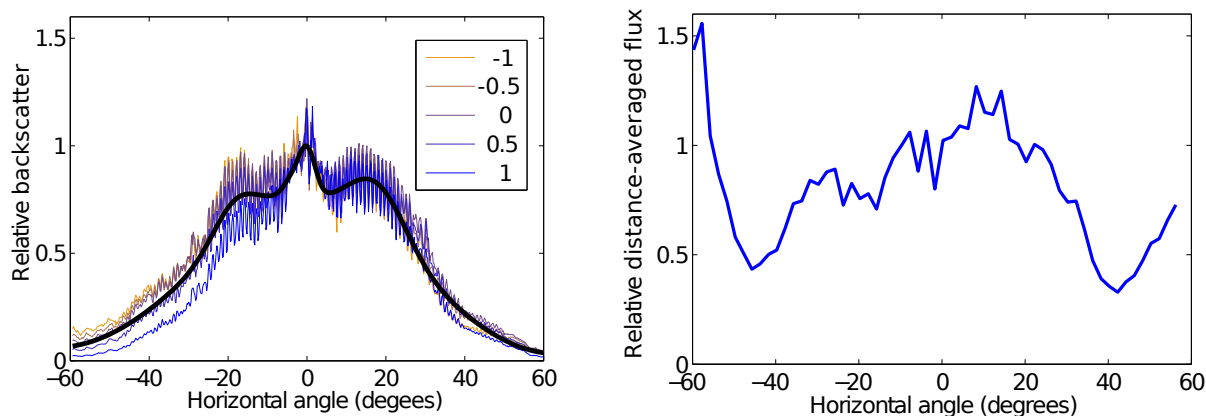

Figure S5: Left: beam pattern from a calibration sphere shows a roughly Gaussian shape. The variability in backscatter across each 1-degree beam corresponds to the sensitivity within each beam. Each line represents the pattern at a different elevation angle (legend in degrees). The black line superimposed is the calibration-sphere beam pattern. Right: average flux values as a function of direction (2° resolution) from the April 2012 data corrected with the uncorrected beam pattern, normalized to the value in the central beams.

When corrected with the calibration-sphere beam pattern intensity, the resulting long-term ebullitive flux data still showed a recognizable residual directional dependence (Fig. S5, right). The symmetry and temporal consistency of the residual directional dependence indicates that it more likely arises from the measurement system than from an actual spatial pattern of ebullition heterogeneity. This suggests that the beam pattern measured with the calibration sphere did not fully account for the field measurements at UML. This discrepancy may be due to the nearby walls in the tank impacting the measured signal, although the beam pattern measurements were carried out at a closer range than any wall reflections. The discrepancy may also arise from differences between the immobile sphere used for calibration and rising bubble targets detected in the lake. Motion of the bubbles may decorrelate the sonar pulse in time, spreading the sonar signal over neighboring beams and reducing the magnitude of the flow rate estimate. This effect is expected to play a larger role in the outer beams. Ultimately, to address this issue, the residual directional dependence of the flux record was used to correct the beam pattern.

3 Analysis of flux magnitudes

3.1 Regimes of the cumulative distribution function

Approximately 98% of the flux measurements follow a lognormal trend over intermediate magnitudes (0.1-100 mg/m^2/day), with parameters log-mean $\mu = 0.62$ and log-standard deviation $\sigma = 1.8$ (Fig. 2**c** in the main text). Smaller and larger flux measurements are fit by lognormal models with smaller variance, $\sigma = 0.5$ and 1.0, respectively. A flux distribution composed of multiple lognormal regimes was also observed at natural hydrocarbon seeps in a marine setting, although in that study the high-flux regime constituted 13% of the flux measurements, compared with $\sim 1\%$ here [11].

3.2 Uncertainty analysis

The uncertainty associated with flux measurements is estimated to be $\sim$70% and is primarily derived from variability and uncertainty in the bubble size distribution (BSD), although the uncertainty in bubble rise speed, source amplitude, beam pattern and instrument noise were considered. The flux may be expressed as:

$$q = cK \sum_{i=1}^{n_{event}} \sum_{j=1}^{n_{ping}} \left(\frac{\overline{\sigma}_{bs}}{R} \right) \tag{S25}$$

$$= \frac{cK}{a_0} \sum_{i=1}^{n_{event}} \sum_{j=1}^{n_{ping}} \left(\frac{a_{\Delta TR}}{B_h(\theta)G} \right), \tag{S26}$$

$$c = \frac{\Delta t_{ping}}{\Delta t_{sample} A}, \tag{S27}$$

where K is the calibration coefficient (L/day/m), Δt_{ping} is the time between pings, n_{ping} is the number of pings in a given event, and Δt_{sample} and A are the duration and observation area of the sample over which the flux is calculated from the sum of n_{event} events. The backscattering is calculated using the instrument-reported sonar amplitude, $a_{\Delta T}$, and the source level amplitude a_0.

The product $n_{ping} \times n_{event}$ is large for most flux estimates presented in this work, and the averaging over so many measurements makes the contribution from instrument noise negligible. However, the parameters K, a_0 and $B_h(\theta)$ all have significant uncertainty. Each is independent and contributes multiplicatively to q, so the relative uncertainty in q can be estimated using propagation of uncertainty:

$$\frac{\text{var}(q)}{q^2} \approx \frac{\text{var}(K)}{K^2} + \frac{\text{var}(a_0)}{a_0^2} + \frac{\text{var}(B_h)}{B_h^2}. \tag{S28}$$

The uncertainty associated with the calibration coefficient K derives from 3 sources: uncertainty in the bubble rise speed u_{rise}, uncertainty in the long-term BSD, and short-term variations in the BSD (Eq. (S17)).

A number of models for bubble rise speed have been developed, and the nature of the bubble interface ("clean" vs. "dirty") can cause discrepancies of up to $\approx$40%. However, in

a study of marine gas fluxes using the same inverse hydroacoustic method, the relative error between 7 different models contributed only 15% relative uncertainty in K and Q [3]. Plumes of rising bubbles may create upwelling velocities that allow bubbles to rise faster than the terminal velocity of an individual bubble. However, for the relatively low flow rates observed in UML ($Q \leq 20$ mL/min), upwelling velocities are observed to be limited to 2 cm/s, less than 10% of the terminal velocity [12]. Thus, we estimate a combined relative uncertainty of 18% for the rise velocity.

The uncertainty in the long-term BSD may be estimated as $\approx 23\%$ using the relative difference in calibration coefficients calculated using BSDs from UML [8] and Lake Kinneret [5]. The final source of uncertainty in K is from short-term variations in the BSD, over timescales larger than the 5-second averaging period used to measure $\overline{\sigma}_{bs}$. We estimate that BSD varies from the long-term mean by up to $\sim 50\%$ in the radius. If these factors have a multiplicative effect, then the combined relative uncertainty is $\sqrt{\text{var}(K)}/K \approx 58\%$.

The relative uncertainty in a_0 is estimated to be $\approx 22\%$ from the variability in values measured across the sonar fan in UML. The relative uncertainty in $B_h(\theta)$ is estimated to be $\approx 36\%$, from the coefficient of variance in the flux-derived correction to the beam pattern (Fig. S5, right) across θ. Using these values in Eq. (S28), we find a combined relative uncertainty of $\sqrt{\text{var}(q)}/q \approx 70\%$. Over long time periods, the large number of bubbles samples will converge towards the system-wide BSD and reduce the uncertainty in K, the primary contributor to the overall uncertainty. However, because of the inverse relationship between K and r, this convergence in BSD does not guarantee that the flux estimates will converge on the long-term average if there is significant variability in the apparent BSD.

3.3   Spatiotemporal variability as a function of scale

The flux estimates from the deployment from February 18–June 1, 2012 were subsampled uniformly in space and time (gridded in space and time) at different spatial and temporal scales, and the fraction of subsamples that fell within $\pm 50\%$ of the long-term, global mean flux of 7 mg/m^2/day are shown in Fig. S6. The fraction of samples in the interval generally increases with larger spatial and temporal scales, reflecting the rate at which larger-scale, longer-duration observations become more likely to represent the overall mean. Some slight non-monotonicity in the trend may be attributed to time periods where the sensor was inactive. The long-duration (40 day) samples converge to 1 in the limit as the spatial scale increases to 8 m, but for finer spatial resolution significant heterogeneity remains. Similarly, the 8-m samples still show significant temporal variability for samples shorter than 10 days.

3.4   Estimation of the radial distribution function

To account for the enhanced importance of events releasing large volumes of gas, the volume-weighted RDF was estimated using the marked pair correlation function [15, Eqn. (5.3.54)] and the mark-sum intensity [15, Eqns. (4.2.20) and (5.2.2)], with the volume of gas released during an event serving as its mark. The isotropized set covariance was estimated numerically for the irregular observation window and used in place of the pair-specific displacement area [16, Eqn. (9.29)]. The method was confirmed as unbiased using simulations of a CSR process on the same domain used by the sonar.
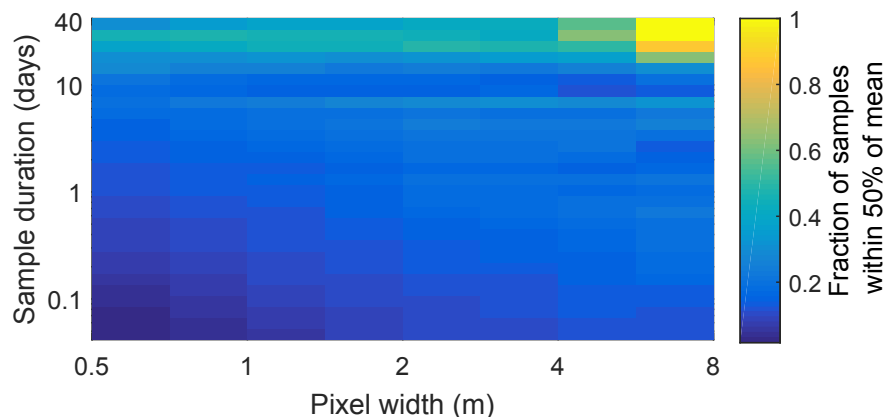
Figure S6: Spatiotemporal variability as a function of scale of measurement. Color scale represent the fraction of subsamples of the data from February 18–June 1, 2012 that fall within ±50% of the long-term, global average flux value, as a function of the spatial extent for gridding of fluxes (0.5-8 m) and duration (1 hr-40 days). Samples shorter than 1 day in duration or with a spatial scale on the order of 1 m (as with most bubble traps) are less than 50% likely to measure a sample within ±50% of the long-term mean. Only multi-week samples with spatial scale over 5 m always fell within ±50%.

Data from Feb 18–May 31, 2012 were divided into segments of 20 min in duration, which were classified as high- or low-flux relative to the average over the whole deployment period. From these segments, continuous samples of durations from 10 min to 4 days were analyzed to test the impact of observation time on the spatial signature observed.

The sonar technique provides sufficient resolution to confirm that the outlets are distinct, as the maximum pixel separation of 0.35 m is finer than the event separation of ≥ 0.5 m, and bubbles are unlikely to drift laterally by more than 0.1 m during their rise of ~ 1.5 m from the sediment surface to the sonar fan, given typical lateral currents on the scale of 1 cm/s (observed from slow, spatially-coherent drift of low-intensity signals reflecting suspended flocs) and bubble rise velocities of $20 - 25$ cm/s [5]. It is possible that non-bubble targets, such as anchor lines, contaminate the RDF sufficiently to create an appearance of spatial clustering in the mean, but these constitute $\leq 6\%$ of the flux so should not create the pronounced effect seen here (Figs. 3d,e in the main text).

Supplemental References

S1. Muyakshin, S. I. & Sauter, E. The hydroacoustic method for the quantification of the gas flux from a submersed bubble plume. *Oceanology* **50**, 1045–1051 (2010).

S2. Weber, T. C. *et al.* Acoustic estimates of methane gas flux from the seabed in a 6000 km² region in the northern Gulf of Mexico. *Geochemistry, Geophysics, Geosystems* **15**, 1911–1925 (2014).

S3. Veloso, M., Greinert, J., Mienert, J. & De Batist, M. A new methodology for quan-

tifying bubble flow rates in deep water using splitbeam echosounders: Examples from the Arctic offshore NW-Svalbard. *Limnology and Oceanography-Methods* **13**, 267–287 (2015).

S4. Anderson, V. C. Sound scattering from a fluid sphere. *Journal of the Acoustical Society of America* **22**, 426–431 (1950).

S5. Ostrovsky, I., McGinnis, D. F., Lapidus, L. & Eckert, W. Quantifying gas ebullition with echosounder: the role of methane transport by bubbles in a medium-sized lake. *Limnology and Oceanography-Methods* **6**, 105–118 (2008).

S6. DelSontro, T., McGinnis, D. F., Wehrli, B. & Ostrovsky, I. Size does matter: Importance of large bubbles and small-scale hot spots for methane transport. *Environmental Science & Technology* **49**, 12681276 (2015).

S7. Medwin, H. & Clay, S. *Fundamentals of Acoustical Oceanography (Applications of Modern Acoustics)* (Academic Press Limited, 1998).

S8. Delwiche, K., Senft-Grupp, S. & Hemond, H. A novel optical sensor designed to measure methane bubble sizes in-situ. *Limnology and Oceanography - Methods* , doi:10.1002/lom3.10060 (2015).

S9. Daszykowski, M., Walczak, B., & Massart, D.L. Density-based clustering for exploration of analytical data. *Analytical and Bioanalytical Chemistry* **380**, 370–372 (2004).

S10. Thomanek, K., Zielinski, O., Sahling, H. & Bohrmann, G. Automated gas bubble imaging at sea floor – a new method of in situ gas flux quantification. *Ocean Science* **6**, 549–562 (2010).

S11. Clark, J. F., Washburn, L. & Emery, K. S. Variability of gas composition and flux intensity in natural marine hydrocarbon seeps. *Geo-Marine Letters* **30**, 379–388 (2010).

S12. Leifer, I. Characteristics and scaling of bubble plumes from marine hydrocarbon seepage in the Coal Oil Point seep field. *Journal of Geophysical Research* **115**, C11014 (2010).

S13. Wik, M., Crill, P. M., Bastviken, D., Danielsson, A. & Norback, E. Bubbles trapped in arctic lake ice: Potential implications for methane emissions. *Journal of Geophysical Research* **116**, G03044 (2011).

S14. Walter Anthony, K. M. & Anthony, P. Constraining spatial variability of methane ebullition seeps in thermokarst lakes using point process models. *Journal of Geophysical Research* **118**, 1015–1034 (2013).

S15. Illian, J., Penttinen, A., Stoyan, H. & Stoyan, D. *Statistical Analysis and Modelling of Spatial Point Patterns* (Wiley, West Sussex, England, 2008).

S16. Ohser, J. & Mcklich, F. *Statistical Analysis of Microstructures in Materials Science* (Wiley, West Sussex, England, 2000).